Atom Probe Tomography Using an Extreme Ultraviolet Trigger Pulse

Benjamin W. Caplins,[1] Ann N. Chiaramonti,[1] Jacob M. Garcia,[1] Norman A. Sanford,[2] and Luis Miaja-Avila[2]
[1)]*National Institute of Standards and Technology, Applied Chemicals and Materials Division, Boulder, CO 80305, United States*
[2)]*National Institute of Standards and Technology, Applied Physics Division, Boulder, CO 80305, United States*

(The author to whom correspondence may be addressed: benjamin.caplins@nist.gov)

(Dated: 21 August 2023)

Atom probe tomography (APT) is a powerful materials characterization technique capable of measuring the isotopically resolved three-dimensional (3D) structure of nanoscale specimens with atomic resolution. Modern APT instrumentation most often uses an optical pulse to trigger field ion evaporation – most commonly, the second or third harmonic of a Nd laser is utilized (*ca.* $\lambda = 532$ nm or $\lambda = 355$ nm). Herein, we describe an APT instrument that utilizes ultrafast extreme ultraviolet (EUV) optical pulses to trigger field ion emission. The EUV light is generated via a commercially available high harmonic generation (HHG) system based on a noble-gas-filled capillary. The centroid of the EUV spectrum is tunable from around 25 eV ($\lambda = 50$ nm) to 45 eV ($\lambda = 28$ nm), dependent on the identity of the gas in the capillary (Xe, Kr, or Ar). EUV pulses are delivered to the APT analysis chamber via a vacuum beamline that was optimized to maximize photon flux at the APT specimen apex while minimizing complexity. We describe the design of the beamline in detail including the various compromises involved. We characterize the spectrum of the EUV light and its evolution as it propagates through the various optical elements. The EUV focus spot size is measured at the APT specimen plane and the effects of misalignment are simulated and discussed. Long-term stability of the EUV source is demonstrated over more than a year. Finally, APT mass spectra are shown demonstrating the instrument's ability to successfully trigger field ion emission from semiconductor (Si, GaN) and insulating materials (Al_2O_3).

Keywords: extreme ultraviolet; atom probe tomography; field ion emission; high harmonic generation

I. INTRODUCTION

The ultimate goal of atom probe tomography (APT) is to measure the identity and position of every atom in a specimen with elemental/isotopic specificity and atomic-scale precision.[1–4] An APT instrument is the union between a point projection microscope and a time-of-flight mass spectrometer (Fig. 1b). In APT a nanoscale needle shaped specimen is electrically biased until just before DC field ion emission occurs, then a trigger pulse initiates the timed emission of ions from the specimen apex. The location of the ion signal on the detector in combination with the sequence of detection events indicates the spatial origin of the ion on the specimen apex and the time-of-flight of the ion determines the mass-to-charge (Fig. 1c). These data can then be used to computationally reconstruct the eroded volume with sub-nanometer precision (Fig. 1d).

For electrically conductive specimens such as metals, nanosecond voltage pulses can be coupled to the specimen apex and trigger field ion emission.[5] However, specimens consisting of materials with poor electrical conductivity do not permit the propagation of fast voltage pulses and these materials cannot be studied effectively with voltage-pulsed APT.[6,7] Early in the development of APT it was known that optical pulses could also be used to trigger field ion emission and in the 1980s several groups demonstrated proof-of-principle optically-pulsed APT measurements using nanosecond lasers.[8–12] Unfortunately, these lasers tended to be unstable and laser pulsing did not become commonplace.

In the 2000s, several groups restarted research into optically-pulsed APT leveraging the vast improvements in laser technology that occurred since the original work in the 1980s. Many new instruments were described with a variety of pulsed laser technologies that varied in repetition rate, pulse energy, photon wavelength, pulse length, and ease-of-use.[13–23] Broadly speaking, despite the many differences, all of these instruments demonstrated that optically-pulsed APT had significant advantages to voltage-pulsed APT; specifically, optically-pulsed APT using pulsed lasers tends to yield higher mass-resolving power in addition to allowing the study of materials that are poor electrical conductors.[14,16] For optical pulses in the near infrared (NIR), visible (Vis), or near ultraviolet (NUV) regions the dominant field ion emission mechanism follows an Arrhenius rate law where the absorbed optical energy is rapidly thermalized into the lattice and provides a thermal pulse (*i.e.* temperature jump) causing a short spike in the ion emission rate.[15,24–26]

While highlighting the benefits of optically-pulsed APT, these early experiments also noted certain limitations. Most notably is the problem known colloquially as 'thermal tails', which degrade the mass-resolving power and cause a subsequent loss in quantification precision. Broadly, 'thermal tails' are believed to be a result of slow cooling of the tip apex following exposure to an optical pulse.[26] Additionally, materials commonly encountered in APT can have a wide range of optical properties in the NIR/Vis/UV regions making it difficult to find a pulse energy (*i.e.* flux or irradiance) that is uniformly successful for all spatially distinct portions of a heterogeneous nanostructure.

To circumvent problems associated with thermal pulsing (via optically-induced thermal transients), research is underway to develop optically pulsed instruments that do not rely on bulk optical absorption mechanisms to impart thermal transients to the APT tip. A team of researchers at the University

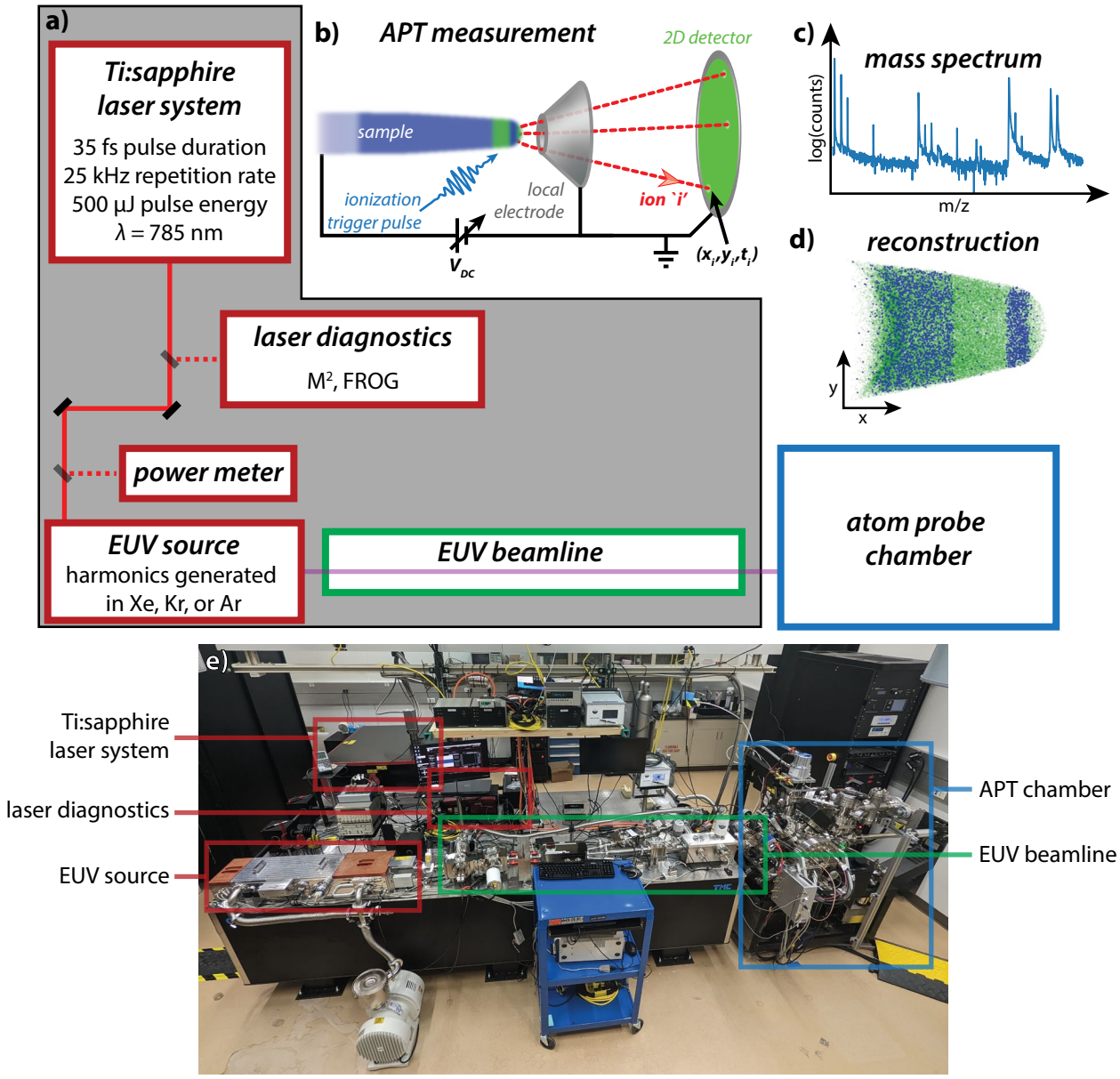

FIG. 1. (a) Schematic experimental layout on an 'L'-shaped laser table. The Ti:sapphire laser serves as the NIR driving field for high harmonic generation in the commercial EUV source. The EUV light is filtered and focused into the atom probe chamber via a vacuum beamline. (b) Schematic of an optically pulsed APT experiment. A DC voltage is applied to the specimen and an optical pulse triggers field ion evaporation. The ion is projected by the electric field to a position sensitive time-of-flight detector where it is analyzed. (c) An example mass spectrum (GaN) that is obtained from an APT experiment. (d) An example 3D reconstruction obtained from an APT experiment on a InGaN heterostructure. (e) The experimental setup as it was implemented with each of the major components identified.

of Rouen recently began development on a system that uses a phase-stable single-cycle THz optical pulse to optically couple a pulsed electric field to the tip.[27] This may circumvent the difficulty in propagating short voltage pulses in poor electrical conductors. A different direction pursued at the National Institute of Standards and Technology (NIST) is to use extreme ultraviolet (EUV) light that may directly photoionize atoms with the absence of a significant thermal transient.[28,29] Both of these concepts are under active research and there are many open questions associated with them. Herein, we present the second generation of an EUV pulsed APT instrument we have developed (the first generation instrument was described briefly in Ref. 30). We describe the experimental apparatus in detail and discuss various design choices that were made with an emphasis on the EUV beamline. Characterization data of the instrument is provided and proof-of-principle APT mass spectra are presented.

II. OVERALL DESIGN

The overall structure of the EUV-pulsed APT instrument is shown in Fig. 1a. A commercial[1] Ti:sapphire laser (KM Labs, RAEA-HP) generates short pulses of NIR light at 25 kHz with with up to a pulse energy of 0.5 mJ. This laser is based on a free-space Ti:sapphire femtosecond oscillator coupled to a cryogenically cooled chirped pulsed regenerative Ti:sapphire amplifier.

The output pulses from the NIR amplifier are characterized with a suite of laser diagnostic instrumentation. The NIR pulse spectrum was measured on a fiber-coupled spectrometer to have a center wavelength of 785 nm with > 30 nm of bandwidth as measured by the full width at half maximum (fwhm). The pulse duration was 35 fs fwhm as measured via the frequency-resolved optical gating (FROG) technique (Mesa Photonics, MP-001.A). The beam quality was monitored via M^2 measurements (Spiricon, BSQ-SP920). The pulse contrast (*i.e.* the ability to amplify and extract isolated pulses from the oscillator) was monitored on a fast photodiode (Thorlabs, Det10A). The pulse energy was measured with a power meter (Coherent, FieldMaxII-TO/PM30). Some measurements are performed routinely such as spectrum, power, and pulse contrast. Other measurements were only performed as-needed such as pulse duration and beam quality.

The NIR pulse is directed into the EUV source (KM Labs, XUUS 5) via two dielectric mirrors (Newport, 20B20UF.25). These mirrors allow alignment of the NIR laser to the EUV source. Additionally, the leak-through from the first mirror is captured on a fast photodiode (Thorlabs, Det10A) for measurements of pulse contrast in addition to serving as a 'start' timing trigger for the APT time-of-flight mass spectrometer. The leak-through from the second mirror is captured on a second photodiode (Thorlabs, SM05PD1A) which monitors the pulse-to-pulse stability of the NIR light. Finally, a third dielectric mirror is placed on a motorized flip mount such that the mirror can be inserted into the beam path in order to direct the beam onto a power meter. The entirety of the beam path between the NIR laser and the EUV source is enclosed in anodized aluminum beam tubes; this serves the dual purpose of keeping the laser operator safe while also reducing air currents that would disturb the beam.

The EUV source actively stabilizes the NIR beam pointing using two piezo controlled mirror mounts and two beam sampling cameras. The NIR pulse is focused into a capillary which contains a controlled pressure of noble gas (Xe, Kr, or Ar). The NIR driving field interacts with the noble gas atoms through a process known as high harmonic generation, and spatially coherent odd harmonics of the NIR driving frequency are produced with a pulse width smaller than the NIR driving field (≈ 10 fs[31]).[32–37] The exact spectrum of the harmonics is dependent on many factors, but in the present system EUV photons in the range of 20 eV to 60 eV are efficiently produced and transmitted. The centroid of the EUV spectrum increases with the ionization potential of the gas and so Ar yields EUV photons of higher energy than Kr, which yields higher energy photons than Xe.[38] The EUV light exits the source and transmits through the beamline (described below) to the APT analysis chamber (Cameca, LEAP 4000X Si) where it is focused onto an atom probe specimen apex. The actual layout of the experimental system is shown in Fig. 1e with each main component labeled.

[1] Commercial instruments, equipment, or materials are identified only to adequately specify certain procedures. In no case does such an identification imply recommendation or endorsement by NIST, nor does it imply that the products identified are the best available for the purpose.

III. EUV BEAMLINE

The NIR driving laser, the EUV source, and the APT instrument are all commercially available and so the focus of this work is on describing the beamline and characterizing the EUV light. The beamline is shown schematically in Fig. 2a and a photo of the beamline is shown in Fig. 2b with all optical elements labeled. Note that many of the beamline components are based on commercially available modules that were selected and customized for the current application. We will begin by discussing the functional requirements of the beamline followed by giving a broad overview of the beamline before discussing how the chosen design meets those goals.

A. Beamline Functional Requirements

Broadly speaking, the beamline needs to fulfill a number of purposes:

- Transmit a sufficient number of EUV photons to trigger field ion emission while maintaining the APT chamber vacuum quality ($\approx 10^{-9}$ Pa or $\approx 10^{-11}$ Torr)
- Block NIR light from reaching the specimen
- Allow for the measurement and modification of EUV pulse energy
- Allow for the characterization of EUV spectrum
- Focus the EUV light onto the APT specimen apex
- Allow for alignment of the EUV light to the APT specimen apex

B. Beamline Overview

The NIR and EUV light exit the capillary propagating collinearly. The residual NIR light is attenuated after striking two flat mirrors (M1 and M2) and any remaining NIR light can be filtered out by aluminum foils (Lebow) held in filter wheels. The remaining EUV light can then take one of two paths depending on the position of the toroid (T1, $f = 600$ mm). When the toroid (T1) is inserted into the beam path the EUV light enters an imaging spectrometer. The imaging spectrometer consists of the toroid (T1), grating (G1) set up for conical diffraction (500/mm and plane-ruled at 4.7°), and CCD camera (Greateyes, ALEX-s 2k512 BI) set up to image

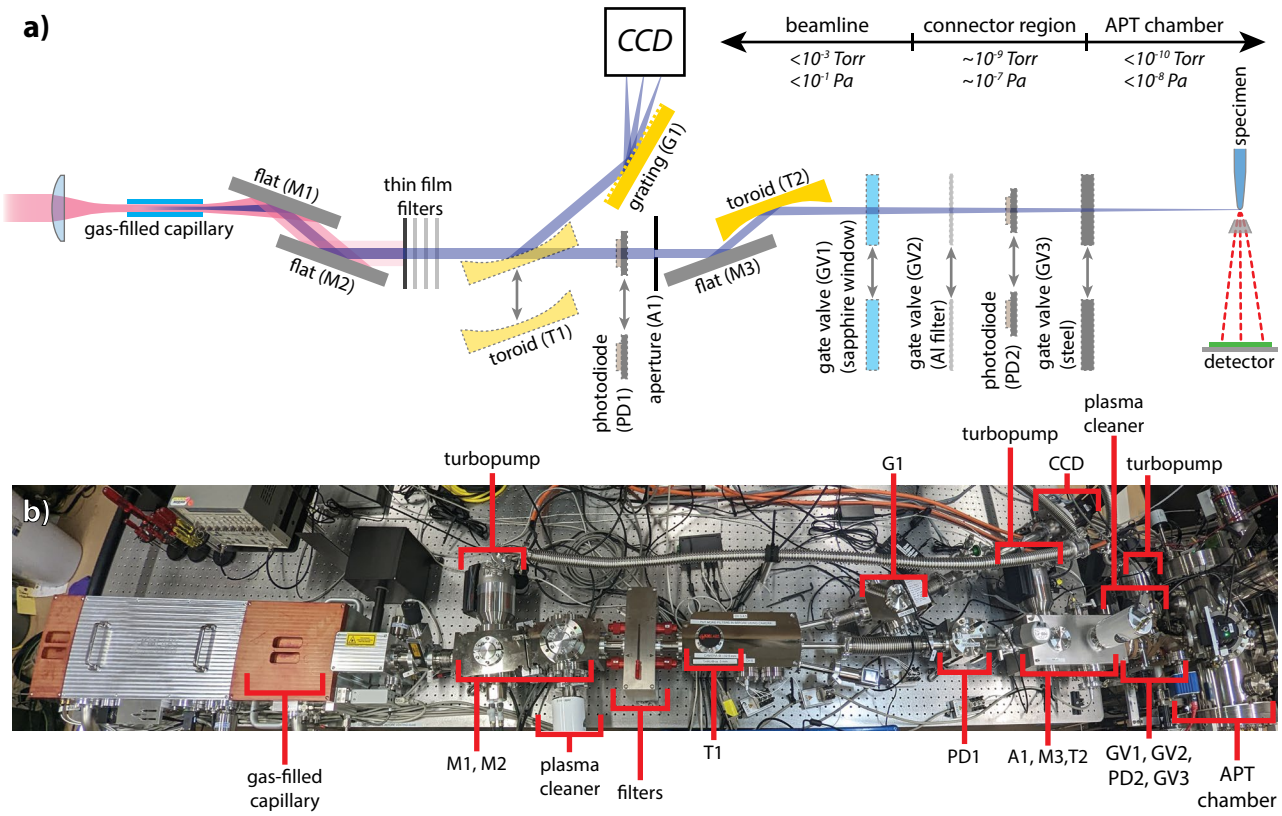

FIG. 2. (a) Schematic of the EUV beamline. The EUV light is generated collinearly with the NIR driving field in a noble gas filled capillary. The EUV light is isolated from the NIR light by means of two flat mirrors (M1 and M2) and Al filters (*i.e.* foils). When a toroid (T1) is inserted into the beam path, the light is reflected from a grating (G1) and focused onto a CCD camera for spectral analysis. When a toroid (T1) is removed from the beam path the EUV light transmits past the toroid and through a circular aperture (A1) before reflecting off a flat mirror (M3) and then a toroid (T2) which focuses the light inside the APT analysis chamber and onto the APT specimen apex. During alignments utilizing NIR light, the ultra high vacuum region is separated from the beamline via a sapphire window mounted on a gate valve (GV1). During experiments with EUV light, the ultra high vacuum analysis region is separated from the beamline via an Al filter mounted on a gate valve (GV2). When the instrument is idle, a standard steel gate valve (GV3) is closed to provide robust isolation between the ultrahigh vacuum chamber and the beamline. Two EUV sensitive photodiodes can be inserted into the beampath (PD1, PD2) for power measurements. The focal spot is steered onto the tip by a computer controlled tip/tilt actuator on which a toroid (T2) is mounted. (b) The beamline setup with each of the major components identified.

the exit of the capillary to the CCD camera in a 1:1 imaging configuration. When the toroid (T1) is removed from the beam path, the beam reflects from a flat mirror (M3) and is focused by the toroid (T2, $f = 400$ mm) onto the APT specimen apex.

Several optical elements can be inserted into the beam path as needed. The two photodiodes (Opto Diode, AXUV100G and SXUV100) can be inserted into the beam path and the resulting photocurrent can be measured on a picoammeter (Keithley, 6485). The manufacturer-supplied responsivity data can then be used to calculate an EUV power and pulse energy. The aperture (A1, 1.9 mm diameter) can be inserted into the beam to limit the numerical aperture of the beam incident on the toroid (T2) and reduce aberrations at the EUV focus. A gate valve (VAT, 01032-UE01-AAT2) with a sapphire window (GV1) can be inserted into the beam path for initial alignment of the beamline. The same type of gate valve (GV2) holding a 200 nm thick, freestanding, pinhole-free Al filter (Luxel) can be inserted into the beam path during APT data collection and serves as a vacuum break between the beamline ($< 10^{-1}$ Pa or $< 10^{-3}$ Torr) and the APT analysis chamber ($< 10^{-8}$ Pa or $< 10^{-10}$ Torr). When experiments are not being performed, a standard steel gate valve (GV3) is inserted to ensure the vacuum integrity of the APT chamber.

C. Beamline Efficiency

EUV light is strongly absorbed by all materials, including gases.[39] Thus, the beamline must be evacuated to $< 10^{-1}$ Pa ($< 10^{-3}$ Torr) to avoid significant absorption losses. Since the capillary is being continuously supplied with noble gas to maintain pressures in the range of 10^3 Pa (10^1 Torr) to 10^4 Pa (10^2 Torr) as required for high harmonic generation, the beamline needs to be actively pumped. To this end, two turbopumps are placed before the sapphire-window gate valve (GV1) to

maintain beamline pressures around $\approx 10^{-2}$ Pa ($\approx 10^{-4}$ Torr) with a third turbopump placed between the sapphire-window gate valve (GV1) and the stainless steel gate valve (GV3) to maintain a pressure of $\approx 10^{-7}$ Pa ($\approx 10^{-9}$ Torr).

The EUV reflectivity of common mirrors at near-normal incidence is typically very small because the complex refractive index is close to unity at these frequencies.[39,40] Two general strategies exist for achieving high optical reflectivity: (1) optics are used at grazing incidence angle[40,41] or (2) multilayer (interference-based) mirrors are used[40,42]. One notable difference between these two types of optics is that grazing incidence optics are intrinsically broadband, while high reflectivity multilayer mirrors designed for EUV light have a narrow bandwidth and generally select a single harmonic to reflect. In the previous generation of the EUV APT system,[30] about half of the optics were chosen to be grazing incidence optics (12° angle of incidence) and half of the optics were chose to be multilayer mirrors (near normal incidence). The theoretical reflection efficiency of the grazing optics was around 80 % and the theoretical reflection efficiency for the multilayer mirrors was around 40 %. By measuring the EUV power before and after the multilayer mirrors, we found that the actual reflectivity of those multilayer mirrors was about an order of magnitude lower than the theoretical reflectivity. It is unclear why this discrepancy existed, though degradation of the optic (oxidation or contamination) in addition to difficulty in matching the spectrum of the harmonics to the reflectivity curve of the optic likely contributed.

In the current system, ensuring the maximum number of photons are delivered to the specimen apex is a priority. Thus, only grazing incidence optics were used, and the angle of incidence was decreased to 6° in order to improve the reflectivity. This choice ensures a broadband reflection with high efficiency. While all mirrors in this system are used at grazing incidence angle, the Al filters are used at normal incidence. Finally, we note that a minimal number of optical elements was used in the design of this beamline – this represents fewer surfaces to absorb the light, fewer surfaces to align, and fewer surfaces to keep clean of contamination/oxidation.

The high EUV irradiance on the filters tends to cause contamination of the surface and, therefore a reduction in the transmission. Similar concerns apply to the surfaces of the reflective optical elements, though this is somewhat mitigated by the larger footprint of the beam on grazing incidence optics. To ensure these surfaces are kept free of contamination, two plasma cleaners (Pie Scientific, EM Kleen) were installed on the beamline (see Fig. 2b) and run on a routine basis using air for the plasma gas.

To summarize, the beamline is evacuated to limit absorption by gases. Broadband, grazing incidence, high-reflectivity EUV optics are used. Surface contamination is minimized with routine plasma cleaning. And finally, a minimal number of optics are used in the beamline (only four mirrors are used for EUV APT experiments).

D. Removing Residual NIR

The NIR (p-pol[2]) and EUV (p-pol) light exits the capillary propagating collinearly and after the capillary there is on the order of 10 W of NIR light and 50 μW of EUV light. This NIR light must be completely removed prior to entering the APT chamber. Additionally, when using the imaging spectrometer the residual NIR light must be removed so as not to overwhelm the CCD and possibly damage the sensor. Traditionally, the removal of the NIR light is done in two steps. First, one or more 'Si brewster plates'[43,44] and/or antireflection coated 'grazing incidence plates'[45–47] are used to reduce the NIR flux by more than an order of magnitude. Then, the remaining NIR light is eliminated with an Al filter.[48] The vastly different optical constants for EUV and NIR light ensure that even a 200 nm thick Al filter will transmit effectively no NIR light as long as the filter is free from pinholes.

In our system the first optical elements following the capillary in the beamline are two flat mirrors (M1 and M2). Both of these mirrors serve as NIR/EUV beamsplitters or 'grazing incidence plates' (KM Labs) that have an antireflective coating designed to transmit the residual NIR driving field to the optical mount while presenting a top coating of Si which efficiently reflects the EUV light.[46,47] The first of these mirrors is exposed to the highest optical power and is fixed directly to a water-cooled block to ensure stability with respect to thermal drift.

Following these mirrors is a set of filter wheels which hold an array of Al filters of different thicknesses. When the beam is reflected into the spectrometer at least one 1 μm thick Al filter is in the beam path as these filters tend to reliably be pinhole free and remove all NIR light. When the beam is transmitted to the APT experiment chamber, the gate valve (GV2) with a 200 nm thick Al filter is always present (since it serves as a vacuum break) and this removes any residual NIR light.

Initial alignment of the beamline is easier to perform with NIR light at atmospheric pressure with the beamline optical elements not anchored to the table. To facilitate this initial alignment a waveplate is placed prior to the capillary and is used to rotate the polarization of the NIR light from p-pol to s-pol. The s-pol NIR light has an increased reflectivity from the flat mirrors and can be viewed with an handheld NIR viewing scope. Once the beamline is roughly aligned, anchored to the table, and evacuated, the sapphire gate valve (GV1) can be inserted instead of the Al filter gate valve (GV2) and the rough alignment into the APT chamber can be accomplished with a NIR viewer. Thus, while under normal conditions the beamline is designed for the elimination of all NIR light, alignment is strongly facilitated by the ability to permit NIR light to transmit through the beamline.

[2] In these experiments when the light is p-pol with respect to the beamline optics it's polarization vector is parallel to the table and parallel to the long axis of the APT tip.

E. Pulse Energy, Filter Transmission, and Source Stability

Pulse energy is a common experimental variable modified during optically triggered APT experiments in addition to being a useful metric for the health of the EUV source. Thus the EUV pulse energy must be able to be routinely measured and modified over many orders of magnitude. As noted above, the measurement of EUV pulse energy is determined from a power measurement made using an EUV photodiode and a picoammeter. We assumed that the manufacturer-supplied responsivity curves are reasonably accurate. Two photodiodes of different types are installed in the system to provide some redundancy in the measurement. The second photodiode was placed after the final EUV optic (GV2) to ensure the most direct measurement of the relevant pulse energy without the need to account for reflection or transmission losses.

As a practical matter, the pulse energy of the source cannot be directly measured because that would require all the Al filters to be removed from the beamline and the photodiode response would be saturated by the residual NIR light. Hence, typically the EUV power is measured after transmitting through a 1 μm thick Al filter. As the filter transmission may change over time, this transmission must also be measured via a ratiometric method if the source output is desired. Briefly, if the transmission of filter 'A' is desired, then a second filter 'B' is needed. The EUV power (*i.e.* photodiode current) is then measured when both 'A' and 'B' are inserted in the beamline and this measurement is divided by the EUV power measured when only 'B' is inserted into the beamline. Note that this approach assumes that the filters have a flat spectral transmission and are pinhole free.

We monitored the transmission of a particular 1 μm thick Al filter using the ratiometric method outlined above. After the initial commissioning of our beamline, it was observed that the filter had been visibly contaminated. The filter transmission was initially measured at 1.9 % transmission (% T) at the beginning of commissioning, and once the visible contamination was noted the filter transmission was measured at 0.8 % T. Running the plasma cleaner for about 100 minutes (placed opposite mirror M2, before the filter wheel) recovered a significant fraction of the transmission and removed the visible contamination (Fig. 3a). Long-term measurements of the filter transmission over roughly 400 days (Fig. 3b) showed a relatively stable transmission (except for a short period of a few weeks where the plasma cleaner was removed from the system) and no further contamination was ever visible by eye.

Over the course of >400 days the photodiode current (proportional to the optical power) was routinely measured after the same 1 μm thick Al filter (Fig. 3c). Around 260 days from the start of recording these data the NIR laser power was reduced from 13.7 W to 12.3 W, which resulted in a modest drop in photodiode current. Normalizing the data for this stepwise change in NIR driving field and dividing by the measured filter transmission (Fig. 3b) yields a metric of the long term source intensity (Fig. 3d). Notably, over the course of the recorded data (roughly 400 days) the coefficient of variation of the source intensity was only 10 % which is more than sufficient for repeatable APT experiments.

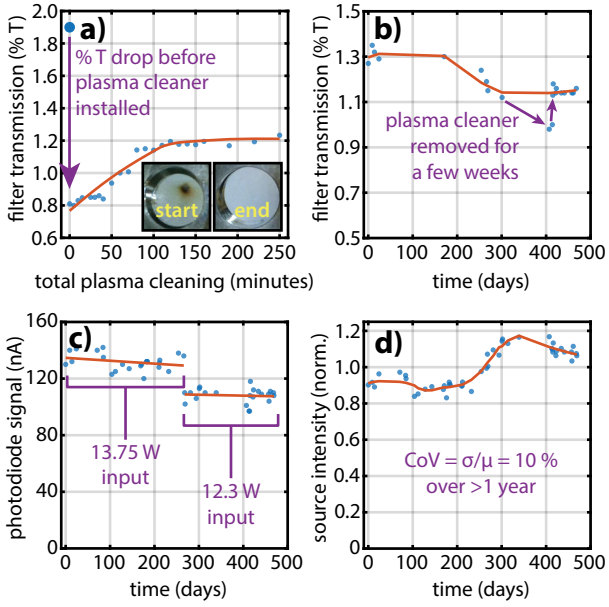

FIG. 3. (a) The transmission of a nominally 1 μm Al filter over time. The initial filter transmission dropped quickly (a few weeks) and a black mark was visible on the filter (inset). Plasma cleaning removed the black mark (inset) and improved the transmission. (b) Routine plasma cleaning maintained a relatively stable filter transmission over more than a year. The drop in transmission between 200 and 300 days is likely related to a small change in the EUV spectrum that can occur following maintenance of the NIR laser. (c) The EUV source was measured on a photodiode in the same configuration over the course of roughly 400 days. When the driving field pulse energy was maintained at the same value the EUV output was stable. (d) A source intensity is plotted by dividing out the known changes in filter transmission and the change due to the driving field pulse energy. Over the course of more than one year the coefficient of variation (CoV) of the source intensity is ≈ 10 %.

For the modification of the pulse energy, Al filters of various thicknesses are placed in the beam path via the filter wheels. The system has four filter wheels installed, and each filter wheel can hold up to seven filters with an eighth spot reserved for free-space (*i.e.* no filter). Filters of thickness ranging from 200 nm to 1 μm were installed and by measuring the transmission through various combinations of these filters the pulse energy could be reduced many orders of magnitude. For example the 1 μm thick Al filters tended to stabilize at 1.2 % T and so four of these would attenuate the pulse energy by $\approx 10^{-8}$. Alternatively, a single 200 nm thick Al filter reduce the pulse energy to ≈ 25 % T. For reference, the maximal pulse energy (*i.e.* with only the Al filter in GV2 inserted) measured on the photodiode directly in front of the APT specimen (PD2) was between 100 pJ and 200 pJ for harmonics generated in Xe, Kr, and Ar.

F. Characterization of EUV Spectrum

The characterization branch of the beamline is distinct from the APT branch and the optics that are encountered on each

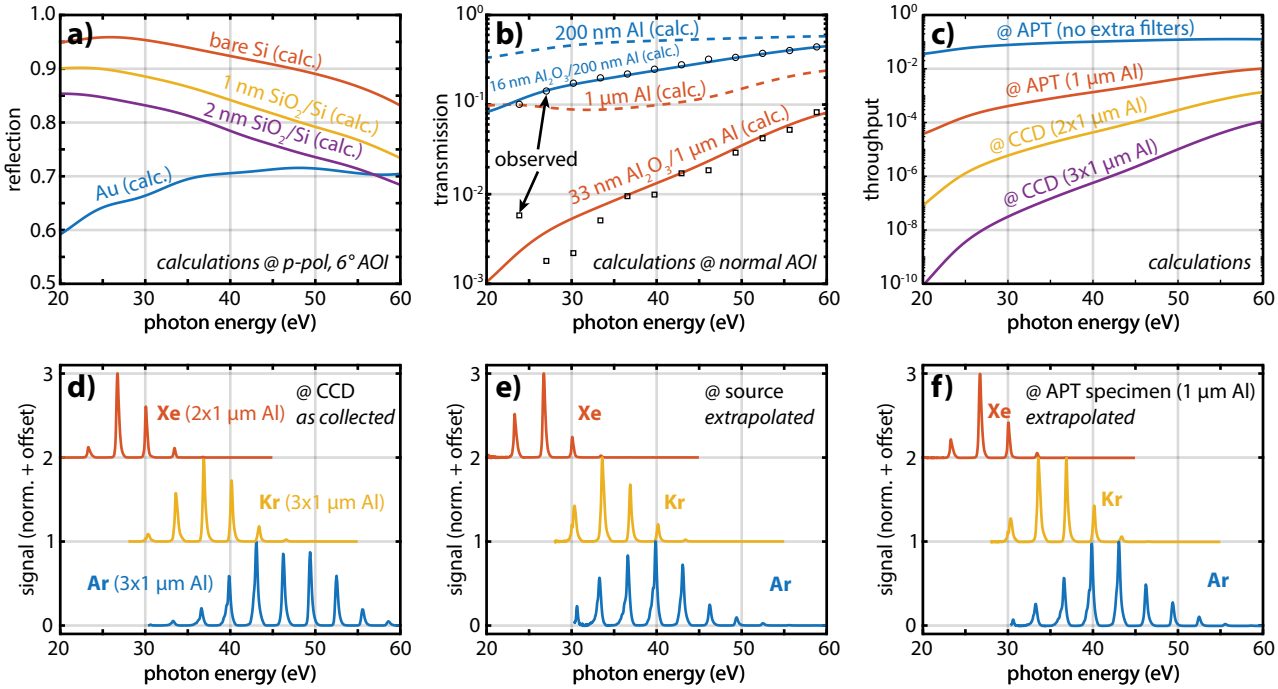

FIG. 4. (a) Calculated reflectivity (p-pol, 6° grazing angle-of-incidence) of the coatings used on the grazing incidence optics present in the beamline. Note that nominally Si coated optics are expected to have a native oxide after exposure to air around 1 nm thick. (b) Calculated transmission (normal angle of incidence) for potentially oxidized Al filters present in the beamline. The dashed lines are calculated for 200 nm and 1 μm thick unoxidized Al. The solid lines are for the same filters with 16 nm and 33 nm of Al_2O_3 added, respectively. The hollow circles and squares show the measured transmission of two Al filters present in the beamline that are nominally 200 nm and 1 μm thick, respectively. (c) Calculated beamline throughput for various configurations including at the CCD camera and at the APT specimen location. Note that these calculations are smoothed by the spacing of the EUV harmonics (3 eV). (d) The spectra 'as collected' on the CCD for EUV light generated with different noble gases with two 1 μm Al filters (Xe) and three 1 μm filters (Kr and Ar). (e) The 'at source' spectra calculated by dividing the 'as collected' spectra by the beamline throughput to the CCD. (f) The 'at APT specimen' spectra calculated by multiplying the 'at source' spectra by the beamline throughput to the APT chamber (with a 1 μm Al filter inserted).

branch differ. Thus, the spectrum that is measured with the imaging spectrometer, is not necessarily the same as that delivered in the APT chamber. In order to understand what the spectrum incident on the APT specimen is, the reflectivity and transmission of each optic should be considered so that the measured spectrum can be numerically corrected for the actual optics in use.

In the present EUV APT system, maximizing the beamline efficiency was deemed more important than selecting a particular EUV harmonic. Thus, as noted above, the beamline was designed to use grazing incidence optics which reflect efficiently over a broad spectral bandwidth. Specifically, the flat mirrors have a top coating of Si, which forms a native oxide layer between 1 nm and 2 nm thick.[49] The toroidal mirrors are gold coated. The reflectivity was calculated using the IMD software package[50] using the tabulated values of the optical constants for Au, Si, and oxidized Si surfaces (p-pol, 6° grazing angle of incidence) and is shown in Figure 4a.[3] The gold reflectivity is biased slightly towards higher photon energies, while the Si reflectivity is biased slightly towards lower photon energy. The native oxide coating on Si appears to have little effect on the slope of the reflectivity curve, though the oxide reduced the overall reflectivity by 10 % to 20 % depending on the thickness. Unfortunately, the grating (G1) reflectivity cannot be easily measured in our system or accurately modeled[54] and so we treat it as a Au mirror and acknowledge that this introduces uncertainty into our calculations.

In addition to the reflective optics, the beamline also utilizes Al filters as transmissive optics. It is well known that Al filters form oxide coatings which can increase in thickness over the course of time.[48,55] In Figure 4b the calculated transmission for unoxidized Al filters (200 nm and 1 μm thick) are plotted. In addition, the measured transmission of the nominally 200 nm and 1 μm thick Al filters are shown. These data were then fit by allowing a variable thickness of oxide to be added to the

[3] The IMD software contains a large library of optical constants built from experiment and theory. Unfortunately, the various datasets do not always agree and it is difficult to know which to select for a calculation (*e.g.* see Ref. 51). Here we tended to use the data from Palik[52,53] with the exception of Al where the CXRO[39] data was used. Specifically, we used the 'Si.nk', 'aSiO2.nk', 'Al_llnl_cxro.nk', 'a-Al2O3_palik.nk', and 'Au_palik.nk' optical constants files from the IMD database with point discontinuities removed.

nominal Al thickness. With only this single free parameter, the data can be reasonably explained. This resulted in a ≈ 16 nm thick Al_2O_3 coating on the 200 nm Al filter, and a ≈ 33 nm thick Al_2O_3 coating on the 1 μm Al filter. This is not intended to be an accurate method for determining the oxide thickness since the phases, micro-structure, and composition of these filters was not explicitly studied, however, these thicknesses are in reasonable agreement to that determined previously for aged Al filters.[48]

Importantly, in contrast to the reflective Si optics where the oxide coating had little impact, the transmission of the Al filters are strongly affected by the oxide in two distinct ways. First, the oxide dramatically lowers the transmission of the filters. Second, the slope of the transmission spectrum is significantly increased with the addition of oxide. The unoxidized 1 μm thick Al filter would be expected to attenuate the spectrum fairly evenly across the 20 eV to 60 eV range of photon energies. In contrast, the oxidized filter attenuates the spectrum by about two orders of magnitude more at 20 eV than at 60 eV. Thus, while the unoxidized Al would be expected to be a fairly good 'neutral density' filter, the oxidized Al filter is a strongly sloped filter and may shift the centroid of the EUV light spectrum.

The calculated throughput for the two beamlines with varying numbers of Al filters inserted into the beam is shown in Fig. 4c. During spectral characterization, two or three 1 μm Al filters are inserted and the resulting throughput is shown. Note that these calculations also include the manufacturer-specified camera quantum efficiency. During APT experiments, it is common to have either no extra Al filters or a single 1 μm filter and the resulting throughput is shown for these configurations. These spectral transfer functions demonstrate at least three important points. First, the APT beamline has a very high overall throughput – up to almost 10 % across the 20 eV to 60 eV spectral range. Second, when the beam is attenuated with Al filters, the spectral response is dominated by the transmission of these filters. Third, the spectral slope of the Al filters causes the transfer functions to be strongly biased towards higher photon energy. Thus, the EUV spectrum measured on the CCD spectrometer is not the same as the spectrum of light incident on the APT specimen.

To discuss the spectrum of the EUV light more concretely, we show representative 'as-collected' spectra in Fig. 4d. The results of numerically correcting these spectra with the transfer functions shown in Fig. 4d are shown in Fig. 4e-f and represent the best estimates of the 'at-source' and 'at-APT specimen' spectra. Notably, the sloped transfer function arising from the Al filters shifts the centroid of the EUV spectra to higher photon energies. For example, the 'as-collected' EUV light generated in Ar yields a centroid around 47 eV, while the 'at-source' estimate has a centroid shifted down to around 40 eV, and the 'at-APT specimen' centroid is estimated to be around 42 eV. Similar shifts occur for EUV light generated in Kr and Xe gas, however, the narrower overall spectral bandwidth of the EUV light generated in those gases limits the effect to be of lower magnitude.

The importance of the exact EUV spectrum for EUV triggered APT is currently unknown. However, the characterization of the EUV spectrum outlined here gives clear bounds on how much the spectra can shift as Al filters are inserted/removed to adjust the EUV pulse energy. Furthermore, from a practical standpoint, it also emphasizes that (wavelength integrated) ratiometric transmission measurements performed on a photodiode, while useful, have limitations.

G. Focusing the EUV Light on the APT Specimen Apex

In the context of an atom probe experiment, the goal is to use the EUV optical pulse to trigger field ion emission from the apex of a nanoscale tip. Thus, the photon flux should be maximized at the tip apex which is $\ll 1$ μm. In the case of high harmonic generation in a capillary, the source size is several tens of micrometers with ≈ 1 mrad divergence half-angle ($1/e^2$) and so the source should be imaged to the APT specimen apex with the largest demagnification possible.[37] Here we choose to use a single toroid to focus the beam where experimentally the image distance is minimized relative to the object distance. Within the constraints of the optical table and the existing commercial APT chamber, this led to a geometric (de)magnification of $M = 0.24$ using a $f = 450$ mm toroid with an image distance of ≈ 550 mm.

Using a single toroid with a non-unity magnification results in notable coma aberration.[56,57] To visualize how this will affect the beam profile at the specimen plane, ray tracing simulations were performed using the Python interface of the XRayTracer software package.[58] The source size and divergence were treated as Gaussian with standard deviations selected to match the experiment (20 μm and 5×10^{-4} radians). When no aperture is included in the beamline a notable coma aberration is present (Fig. 5a) which results in a highly asymmetric beam profile. This is a potential problem since ionizing radiation will also strike far away from the specimen apex (*e.g.*, the APT local electrode) and potentially cause unwanted signals. When a 1.9 mm diameter aperture (A1) is included in the beamline simulation (Fig. 5b) then the total photon fluence is reduced to 31 % of its previous value, while the peak fluence is reduced to 80 % of its previous value. Importantly, the beam profile becomes spatially compact and nearly symmetric. Thus, including an aperture in the beamline better directs photons towards the tip while only resulting in a small reduction in the peak photon fluence.

The beamline was initially aligned by physically moving the entire APT chamber with a crowbar until the proper focus was achieved. To facilitate this rough alignment the beamline and APT chamber are mechanically decoupled with a short length of laser welded bellows (Metal-Flex Welded Bellows). However, when APT specimens are changed and APT local electrodes are replaced the specimen apex can move by up to a few hundred micrometers. To accommodate these changes, the beamline needs a highly precise and controlled method of translating the focus at the specimen plane. To accomplish this, we utilize a stick/slip piezo-driven tip/tilt/rotate vacuum actuator (SmarAct, SNM-KML-STT-SR-V2) to control the in-vacuum optics including the toroid (T2). The tip/tilt motions move the beam horizontally and vertically at the speci-

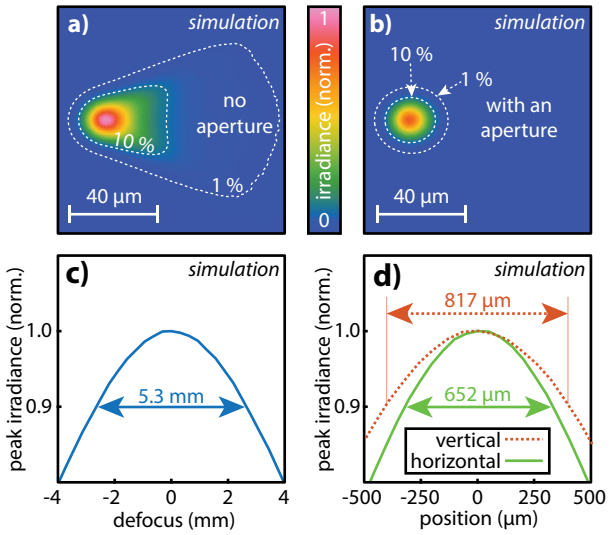

FIG. 5. Simulated (ray traced) irradiance at the APT specimen location showing the beam profile with (a) and without (b) the inclusion of the 1.9 mm diameter aperture (A1). The aperture limits the effect of aberration on the focal spot. (c) Simulation of the peak irradiance (including the aperture, A1) as a function of distance from the optimal focal plane. (d) Simulation of the peak irradiance (including the aperture, A1) as the focal spot is moved horizontally and vertically using the tip/tilt degrees of freedom on the toroid (T2). The peak irradiance is maintained within 10 % of the maximal value for errors in excess of 300 µm.

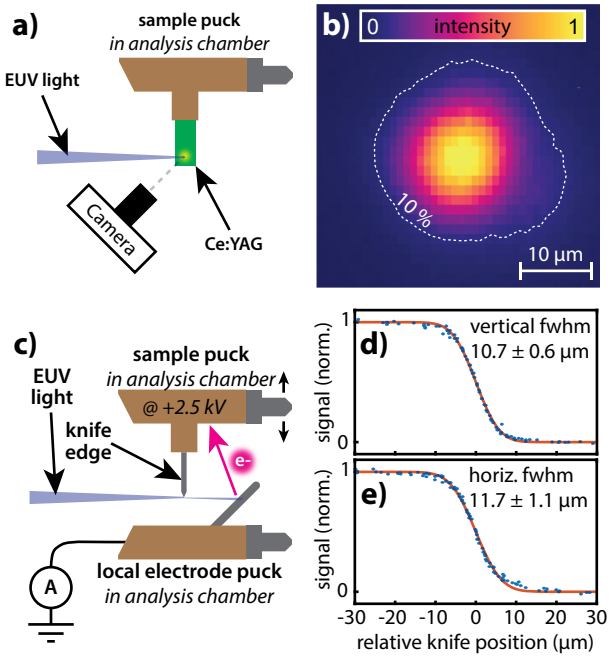

FIG. 6. (a) Schematic of a 2D beam profile measurement. The EUV light strikes a Ce:YAG crystal and the fluorescence is imaged onto a CCD camera at a $\approx 45^\circ$ viewing angle. (b) An example 2D beam profile after the image is corrected for viewing angle. Here the beam size is comparable to the resolution of the camera imaging optics making quantitative analysis difficult. (c) Schematic of a 'knife-edge' beam profile measurement. Here a grounded local electrode puck was modified to have a flat metal surface intersect the beam. A piece of razor blade is mounted on a specimen puck held at +2.5 kV and slowly translated through the beam as the photoemission current is measured. The resulting one-dimensional profiles (d-e) are fit to a Gaussian beam model to extract the fwhm parameters.

men plane. Notably, when selecting these actuators it is important to keep in mind that the vertical movement is demagnified roughly 10× relative to the horizontal movement for a given change in tip/tilt angle due to the grazing incidence geometry.

Using the piezo actuators to change the tip/tilt of the toroid necessarily results in a misalignment of the toroid with respect to the incoming beam which may degrade the focus. Ray tracing simulations were used to verify that the EUV focus would not degrade significantly under typical situations. The peak irradiance is plotted as a function of distance from the focal plane (Fig. 5c) and misalignment from the ideal design alignment (Fig. 5d). These simulations show that once the initial alignment is performed, the day-to-day deviations on the order of up to ± 300 µm can be tolerated with only a small (< 10 %) effect on the peak irradiance.

While ray tracing simulations can be useful for exploring how various parameters can affect the beam profile, the beam profile must also be directly measured at the specimen plane. Here we present two different methods for inspecting the beam profile. In the first method, a Ce-doped yttrium aluminum garnet (Ce:YAG) scintillator crystal is mounted on an APT specimen puck and loaded into the specimen position (Fig. 6a). The EUV beam strikes the crystal causing it to fluoresce. A camera that is typically used for APT specimen alignment is then utilized to collect an image of the beam.[59] The camera is at a 45° angle with respect to the incoming beam and so the resulting image is distorted. A coordinate system for the image is derived from the encoded APT specimen stage by translating the crystal a known amount in each direction orthogonal to the incident beam. The resulting irradiance map (Fig. 6b) shows a nearly circularly symmetric beam with a ≈ 12 µm fwhm. This florescence imaging based method was used during initial alignments of the beam where the overall beam profile shape was of interest, however the resolution of the imaging optics is only slightly better than the beam size and so the deconvoluted beam size is uncertain.

To address the uncertainty in the imaging based method, we developed a second beam profiling technique based on a variation of the 'knife-edge' technique.[60–62] Generally, for a knife edge measurement, a signal proportional to the transmitted power is measured as a sharp edge is translated through the beam (Fig. 6c). The resulting signal as a function of edge position can be fit to a Gaussian beam model and the fwhm can be calculated (Fig. 6d). In the present work, we use small pieces of a razor blade (line edge roughness $\ll 1$ µm as verified in an SEM) mounted on APT specimen pucks to serve as a horizontal and vertical knives. The relative amount of EUV light transmitted past the knife edge was determined by using a picoammeter to measure the photocurrent emitted from

a modified local electrode puck. When the EUV power was reduced to give a linear response, the quantum yield for electron emission was measured as 4.5 % which is in reasonable agreement with literature values for Ni surfaces.[63,64] When this knife-edge method was used to measure the profile of the EUV light generated in Ar gas, the horizontal fwhm was 11.7 $\pm$ 1.1 µm and the vertical fwhm was 10.7 $\pm$ 0.6 µm. The $\approx$ 1 µm uncertainty was derived from the standard deviation of repeated measurements ($n = 6$).

We note that there are other optical designs that could possibly yield better focusing conditions. For instance, zone plates can focus EUV light with a large effective numerical aperture,[62,65] however their short working distance, chromatic aberration, and optic cost make them inappropriate for our application at present. Alternatively, replacing the single toroidal imaging optic with an ellipsoidal optic would lessen the need for a beam limiting aperture and increase the overall transmission,[61] but the added cost was deemed not worth the benefit. Finally, multi-toroid imaging systems can increase the demagnification while keeping a long working distance and minimal coma,[57] but these systems were not yet explored in the current system in order to keep the alignment complexity low.

To summarize, here we used a single toroidal optic (T2) with a (de)magnification of $M = 0.24$ and a $\approx$ 550 mm working distance to image the EUV source onto the APT specimen. An aperture placed before the toroid limits the effect of coma aberration on the focus spot. The alignment of the EUV focus onto the specimen apex is accomplished by computer controlled tip/tilt actuators on the toroid mount and ray tracing calculations show that under normal operating conditions the peak irradiance is reasonably well-maintained during these actions. Finally, the beam profile at the specimen position was measured to be well-approximated by a symmetric Gaussian with a $\approx$ 11 µm fwhm.

IV. APT INTEGRATION

A. Tip Alignment

A notable practical concern that arises when incorporating a new light source onto an atom probe tool is how the user aligns the beam onto the specimen. For the visible or NUV wavelengths commonly employed in APT this is straightforward – the user can easily see on the available specimen cameras when light is scattering off the specimen. In the EUV regime, the scattered light cannot transmit out of the vacuum chamber and so this signal is not available to aid in alignment. Thus, when preparing for an experiment, a specimen puck with a Ce:YAG crystal is loaded into the analysis chamber and the crystal is carefully aligned to the specimen apex position. For this purpose, the Ce:YAG crystal must have a back bevel with a sharp edge that allows a close approach ($<$ 50 µm) to the local electrode. Once the Ce:YAG crystal is in place then the EUV location can be visualized with the EUV induced photoluminescence and moved to the future tip location. Then the Ce:YAG puck is removed and the specimen puck is introduced into the analysis chamber and carefully aligned such that the tip is coincident to where the EUV spot was visualized on the Ce:YAG.

Once this initial beam alignment is performed then the standing voltage is turned on and the data collection is started. As soon as a reasonable detection rate is obtained then the piezo actuators on the toroid (T2) optic are scanned in an attempt to maximize the detection rate. Here we are careful to exclude events < 1 m/z as these typically result from photons scattering directly onto the detector. It is assumed that the maximum detection rate coincides with placing the peak fluence at the tip apex. These piezo scans are repeated after fine tuning the tip to local electrode alignment and/or as necessary during data collection. A combination of the relatively large beam size ($\approx$ 11 µm fwhm) and the stability of the EUV source ensures that tip scans are not necessary more than a handful of times during a typical APT experiment.

B. Scattered Light

One final concern worth noting is that of scattered EUV light. In contrast to photon energies commonly employed in APT to date (3.5 eV and 2.3 eV) EUV photon energies are much greater than the work function for all known materials. For example the stainless steel of the vacuum chamber has a work function in the vicinity of 4.3 eV[66] and so it may be expected that EUV photons scattered on the vacuum chamber walls might generate secondary electrons. In fact, experimentally the photoemission yield from Fe-based surfaces is known to be on the order of 5 % in the EUV regime.[67] In an APT chamber the chamber surfaces are typically at ground potential while the specimen stage is held at a high positive potential and so photoemitted electrons from the chamber walls can accumulate several keV of energy and may contribute a source of noise/artifacts to the measurements. *Thus, the photons that are not absorbed by the specimen should be carefully considered when designing an EUV APT system.* In our work, it was convenient to place a custom beamstop on the specimen puck to absorb the photons that are not absorbed by the specimen since this ensures photoelectrons are generated at the highest positive potential in the chamber and will have a lower probability of generating secondary ions or reaching the detector region.

In addition we note that EUV photons are capable of triggering events on microchannel plates with non-negligible probability (*ca.* 10 %).[68] And so the scattered light signal on the detector should be monitored to ensure it is not overwhelming the detector. To this end, the specimen mounts and tip geometry should be chosen with an eye towards limiting the scattered light striking the detector. Finally, we note that a reflectron-type, time-of-flight detector might be a good fit for future EUV triggered APT systems since it should eliminate the line of sight from the specimen to the detector.

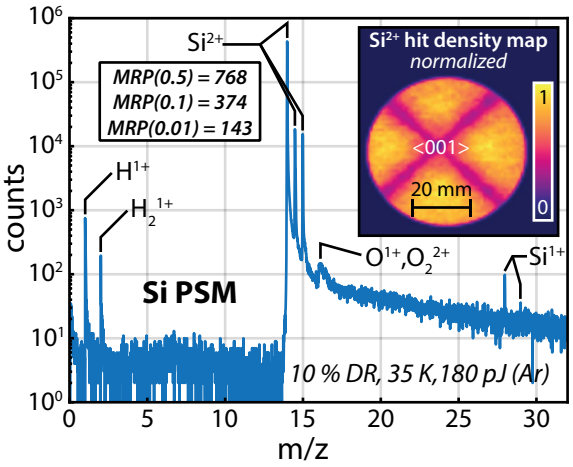

FIG. 7. An EUV triggered APT mass spectrum collected on a commercial Si presharpened microtip plotted with 0.01 m/z binning. The EUV light (encompassing roughly 7 EUV harmonics which spanned 30 eV to 55 eV) was generated with Ar gas, the detection rate (DR) was maintained at 10 %, the specimen temperature was 35 K, and 100 % of the usable EUV flux was used (*i.e.* no extra Al filters were inserted) corresponding to an EUV pulse energy of 180 pJ. The mass resolving power for the Si^{2+} peak calculated at the half, tenth, and hundredth maximum values are shown (as measured for Si^{2+}, SV≈ 6700 V, 90 mm flight length). The Si crystallographic pole is visible in the Si^{2+} hit density map.

V. EUV TRIGGERED APT MASS SPECTRA

We demonstrated the successful collection of EUV triggered APT data on several specimens starting with a Si presharpened microtip (Cameca). Silicon microtips are a good test specimen for demonstrating correct operation of APT instrumentation.[69] In this case the data was collected using the full EUV flux generated with Ar gas (*ca.* 42 eV) and the detection rate was set to 10 %. The mass spectrum of the Si tip (Fig. 7) shows the expected peaks corresponding to Si^{2+} in addition to a low number of H_n^{1+}, Si^{1+}, O_n^{n+} counts. The signal-to-noise ratio is about 10^5 and this permits the observation of a tail on the Si^{2+} peaks which would have been below the noise floor in the previous generation of the EUV APT system. This tail in conjunction with a Si^{2+}/Si^{1+} charge state ratio (CSR) in excess of 10^3 is indicative of a high electric field[70] causing delayed evaporation after exposure to EUV light. The mass resolving power is the ratio of the peak m/z to the peak width and is diagnostic of the instrument performance. Here we measured the mass resolving power on the Si specimen as 768, 374, and 143 using the full width at half maximum, full width at tenth maximum, and full width at hundredth maximum definitions. The mass resolving power is not meaningfully different from the commercially available 355 nm LEAP 4000X-Si tool[71] and indicates that the modifications to the instrument to permit EUV triggered operation did not notably degrade the timing precision nor notably broaden the peaks. Finally, we note that the hit density map for Si^{2+} ions shows the four-fold symmetry expected for <100> oriented single crystal Si.

As a second demonstration specimen we chose GaN as it was studied previously with the first generation EUV APT system.[72] Fig. 8a shows representative mass spectra from a GaN specimen at two different EUV pulse energies using harmonics generated in Ar gas (*ca.* 42 eV). The top spectrum was collected using a 0.5 pJ pulse energy while the bottom spectrum was collected with a 15 pJ pulse energy. The GaN hit density map is shown in Fig. 8b and shows the sixfold symmetry expected for <0001> orientation. In these data, the voltage control loop was set to yield an evaporation rate of 0.5 % and so as the EUV pulse energy is increased the voltage/electric field decreases. The electric field at the tip[73] is monitored by the Ga^{2+}/Ga^{1+} charge state ratio. Previous work using NUV APT found that the measured Ga composition deviated from the expected 50 at.% around a 0.1 CSR.[74–79] In contrast, our previous work using the first generation EUV APT instrument suggested this might not occur for EUV trigger pulses;[72] however, the first generation system did not permit us to explore a wide range of CSRs. With the notable improvements made to the present EUV APT instrument, we were able to collect (apparent) Ga composition data over a much wider range of Ga CSRs and these were plotted with the data from the first generation instrument in Fig. 8c. Notably, the expanded EUV pulse energy in the present instrument allowed us to determine that the same Ga composition bias occurs when using EUV light as occurs when using NUV light. This is in support of the hypothesis that it is the electric field at the tip that controls the compositional bias in GaN.[79]

As a final example we collected data on a sapphire specimen. The mass spectrum is shown in Fig. 9 and the peaks are assigned. In contrast to the previous data, the data on sapphire was collected using EUV light using Xe generated harmonics (*ca.* 27 eV). The data was collected with a 1 % detection rate using a pulse energy of 3.6 pJ. The peaks match up well with the literature assignments.[80] The inset of Fig. 9 shows the hit density map.

VI. CONCLUSIONS

Herein we describe a second generation EUV APT instrument with significantly improved performance, diagnostics, and controls. While the first generation instrument had a repetition rate of 10 kHz and a maximum EUV pulse energy 0.5 pJ, the instrument described herein has a repetition rate of 25 kHz and a maximum pulse energy in the range of 100 pJ to 200 pJ. Additionally, the spot size has been reduced by at least a factor of 2 versus the previous generation instrument. The 2.5× faster repetition rate and 1600× higher EUV flux at the specimen results in a significantly improved APT data collection rate. Furthermore, the present instrument allows for the characterization and modification of the EUV spectrum incident on the specimen in addition to the ability to modify/measure the pulse energy and measure the beam profile at the specimen plane. Finally we describe various practical concerns such as the potentially deleterious effect of scattered light and the alignment of the EUV spot on the specimen apex. Data from

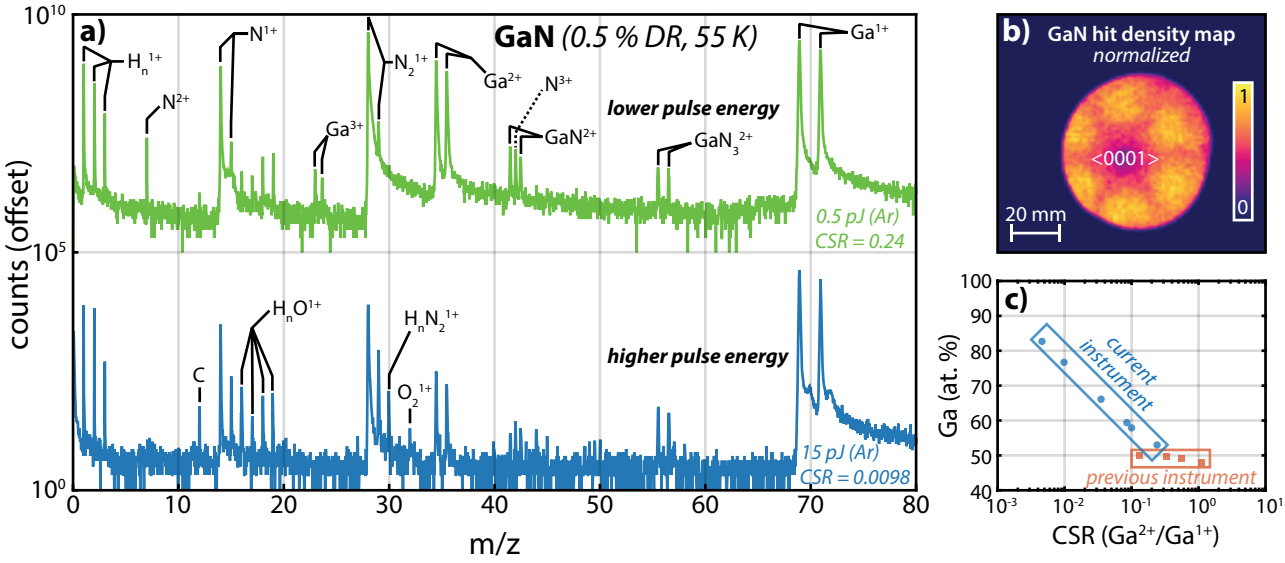

FIG. 8. (a) EUV triggered mass spectra collected on a GaN specimen tip at two different pulse energies with 0.5 % detection rate. The standing voltages were approximately 5100 V and 3000 V for the low and high pulse energy data respectively. The EUV light (encompassing roughly 7 EUV harmonics which spanned 30 eV to 55 eV) was generated with Ar gas. Note that the charge state ratio (CSR) of the Ga peaks are very different. (b) The GaN crystallographic pole is visible in the detector hit density map. (c) The apparent Ga at.% is plotted versus Ga CSR. The current instrument's EUV photon flux is notably higher than the previous version of the instrument and allows for measurements at a much lower Ga CSR (*i.e.* much lower surface electric field).

several materials including GaN, Si, and Al_2O_3 demonstrate the EUV APT instrument is fully functional. Future studies using this second generation EUV triggered APT instrument will seek to elucidate the possible field ion emission mechanisms and understand the possible benefits and/or drawbacks of using EUV light for optically pulsed APT experiments.

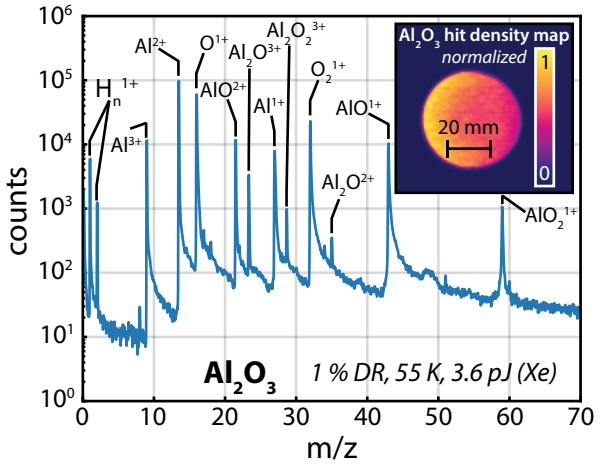

FIG. 9. An EUV triggered APT mass spectrum collected on a Al_2O_3 tip. The EUV light (encompassing roughly 4 EUV harmonics which spanned 25 eV to 35 eV) was generated using Xe gas, the detection rate was maintained at 1 %, the specimen temperature was 55 K, and the pulse energy was 3.6 pJ. The ion hit density map is shown in the inset.

ACKNOWLEDGMENTS

We thank Daniel Hickstein, Seth Cousin, and Clayton Bargsten for their help in the design of the EUV beamline. We thank Thomas Kelly, Kent Rochford, and Marla Dowell for support of this project since its inception. We thank David Diercks for preparing the sapphire sample. We thank Ryan White for assistance with laboratory automation and control. We gratefully acknowledge financial support from the NIST Innovations in Measurement Science Program and technical support from CAMECA Instruments through a cooperative research and development agreement. This work was performed while J.M.G. held a National Research Council Postdoctoral Associateship.

Contribution of NIST, an agency of the US government; not subject to copyright in the United States.

CONFLICTS OF INTEREST

A.N.C. and N.A.S. are inventors on a patent assigned to the United States government and the Colorado School of Mines – US 9,899,197 B2 – that involves the use of extreme ultraviolet light in atom probe tomography.

DATA AVAILABILITY STATEMENT

The data that support the findings of this study are available from the corresponding author upon reasonable request.

[1] B. Gault, M. P. Moody, J. M. Cairney, and S. P. Ringer, *Atom Probe Microscopy*, Springer Series in Materials Science, Vol. 160 (Springer New York, New York, NY, 2012).

[2] D. J. Larson, T. J. Prosa, R. M. Ulfig, B. P. Geiser, and T. F. Kelly, *Local Electrode Atom Probe Tomogr.* (Springer New York, New York, NY, 2013).

[3] M. K. Miller and R. G. Forbes, *Atom-Probe Tomography* (Springer US, Boston, MA, 2014).

[4] W. Lefebvre-Ulrikson, F. Vurpillot, and X. Sauvage, *Atom Probe Tomography* (Elsevier, Cambridge, MA, 2016).

[5] E. W. Müller, J. A. Panitz, and S. B. McLane, "The Atom-Probe Field Ion Microscope," Rev. Sci. Instrum. **39**, 83–86 (1968).

[6] S. J. Sijbrandij, D. J. Larson, and M. K. Miller, "Atom Probe Field Ion Microscopy of High Resistivity Materials," Microsc. Microanal. **4**, 90–91 (1998).

[7] T. F. Kelly, T. T. Gribb, J. D. Olson, R. L. Martens, J. D. Shepard, S. A. Wiener, T. C. Kunicki, R. M. Ulfig, D. R. Lenz, E. M. Strennen, E. Oltman, J. H. Bunton, and D. R. Strait, "First Data from a Commercial Local Electrode Atom Probe (LEAP)," Microsc. Microanal. **10**, 373–383 (2004).

[8] G. L. Kellogg and T. T. Tsong, "Pulsed-laser atom-probe field-ion microscopy," J. Appl. Phys. **51**, 1184–1193 (1980).

[9] T. T. Tsong, S. B. McLane, and T. J. Kinkus, "Pulsed-laser time-of-flight atom-probe field ion microscope," Rev. Sci. Instrum. **53**, 1442–1448 (1982).

[10] W. Drachsel, S. Nishigaki, and J. Block, "Photon-induced field ionization mass spectroscopy," Int. J. Mass Spectrom. Ion Phys. **32**, 333–343 (1980).

[11] T. T. Tsong, Y. Liou, and S. B. McLane, "Methods for a precision measurement of ionic masses and appearance energies using the pulsed-laser time-of-flight atom probe," Rev. Sci. Instrum. **55**, 1246–1254 (1984).

[12] A. Cerezo, C. R. M. Grovenor, and G. D. W. Smith, "Pulsed laser atom probe analysis of semiconductor materials," J. Microsc. **141**, 155–170 (1986).

[13] L. Renaud, P. Monsallut, P. Benard, P. Saliot, G. D. Costa, F. Vurpillot, and B. Deconihout, "The New Laser assisted Wide Angle Tomographic Atom Probe," Microsc. Microanal. **12**, 1726–1727 (2006).

[14] B. Gault, F. Vurpillot, A. Vella, M. Gilbert, A. Menand, D. Blavette, and B. Deconihout, "Design of a femtosecond laser assisted tomographic atom probe," Rev. Sci. Instrum. **77**, 043705 (2006).

[15] J. H. Bunton, J. D. Olson, D. R. Lenz, and T. F. Kelly, "Advances in Pulsed-Laser Atom Probe: Instrument and Specimen Design for Optimum Performance," Microsc. Microanal. **13**, 418–427 (2007).

[16] C. Oberdorfer, P. Stender, C. Reinke, and G. Schmitz, "Laser-Assisted Atom Probe Tomography of Oxide Materials," Microsc. Microanal. **13**, 342–346 (2007).

[17] P. Stender, C. Oberdorfer, M. Artmeier, P. Pelka, F. Spaleck, and G. Schmitz, "New tomographic atom probe at University of Muenster, Germany," Ultramicroscopy **107**, 726–733 (2007).

[18] M. Gruber, C. Oberdorfer, P. Stender, and G. Schmitz, "Laser-assisted atom probe analysis of sol–gel silica layers," Ultramicroscopy **109**, 654–659 (2009).

[19] R. Schlesiger, C. Oberdorfer, R. Würz, G. Greiwe, P. Stender, M. Artmeier, P. Pelka, F. Spaleck, and G. Schmitz, "Design of a laser-assisted tomographic atom probe at Münster University," Rev. Sci. Instrum. **81**, 043703 (2010).

[20] K. Hono, T. Ohkubo, Y. Chen, M. Kodzuka, K. Oh-ishi, H. Sepehri-Amin, F. Li, T. Kinno, S. Tomiya, and Y. Kanitani, "Broadening the applications of the atom probe technique by ultraviolet femtosecond laser," Ultramicroscopy **111**, 576–583 (2011).

[21] L. Zhao, A. Normand, J. Houard, I. Blum, F. Delaroche, O. Latry, B. Ravelo, and F. Vurpillot, "Optimizing Atom Probe Analysis with Synchronous Laser Pulsing and Voltage Pulsing," Microsc. Microanal. **23**, 221–226 (2017).

[22] J. Houard, A. Normand, E. Di Russo, C. Bacchi, P. Dalapati, G. Beainy, S. Moldovan, G. Da Costa, F. Delaroche, C. Vaudolon, J. M. Chauveau, M. Hugues, D. Blavette, B. Deconihout, A. Vella, F. Vurpillot, and L. Rigutti, "A photonic atom probe coupling 3D atomic scale analysis with in situ photoluminescence spectroscopy," Rev. Sci. Instrum. **91**, 083704 (2020).

[23] P. Stender, H. Solodenko, A. Weigel, I. Balla, T. M. Schwarz, J. Ott, M. Roussell, Y. Joshi, R. Duran, M. Al-Shakran, T. Jacob, and G. Schmitz, "A Modular Atom Probe Concept: Design, Operational Aspects, and Performance of an Integrated APT-FIB/SEM Solution," Microsc. Microanal. **28**, 1168–1180 (2022).

[24] A. Cerezo, G. D. W. Smith, and P. H. Clifton, "Measurement of temperature rises in the femtosecond laser pulsed three-dimensional atom probe," Appl. Phys. Lett. **88**, 154103 (2006).

[25] F. Vurpillot, J. Houard, A. Vella, and B. Deconihout, "Thermal response of a field emitter subjected to ultra-fast laser illumination," J. Phys. D. Appl. Phys. **42**, 125502 (2009).

[26] T. F. Kelly, A. Vella, J. H. Bunton, J. Houard, E. P. Silaeva, J. Bogdanowicz, and W. Vandervorst, "Laser pulsing of field evaporation in atom probe tomography," Curr. Opin. Solid State Mater. Sci. **18**, 81–89 (2014).

[27] A. Vella, J. Houard, L. Arnoldi, M. Tang, M. Boudant, A. Ayoub, A. Normand, G. Da Costa, and A. Hideur, "High-resolution terahertz-driven atom probe tomography," Sci. Adv. **7** (2021), 10.1126/sciadv.abd7259.

[28] N. A. Sanford, A. C. Debay, B. P. Gorman, and D. R. Diercks, "Hybrid Extreme Ultraviolet Imaging Spectrometer," (2018).

[29] A. N. Chiaramonti, L. Miaja-Avila, B. W. Caplins, P. T. Blanchard, D. R. Diercks, B. P. Gorman, and N. A. Sanford, "Field Ion Emission in an Atom Probe Microscope Triggered by Femtosecond-Pulsed Coherent Extreme Ultraviolet Light," Microsc. Microanal. **26**, 258–266 (2020).

[30] A. N. Chiaramonti, L. Miaja-Avila, P. T. Blanchard, D. R. Diercks, B. P. Gorman, and N. A. Sanford, "A Three-Dimensional Atom Probe Microscope Incorporating a Wavelength-Tuneable Femtosecond-Pulsed Coherent Extreme Ultraviolet Light Source," MRS Adv. **4**, 2367–2375 (2019).

[31] L. Miaja-Avila, C. Lei, M. Aeschlimann, J. L. Gland, M. M. Murnane, H. C. Kapteyn, and G. Saathoff, "Laser-Assisted Photoelectric Effect from Surfaces," Phys. Rev. Lett. **97**, 113604 (2006).

[32] A. McPherson, G. Gibson, H. Jara, U. Johann, T. S. Luk, I. A. McIntyre, K. Boyer, and C. K. Rhodes, "Studies of multiphoton production of vacuum-ultraviolet radiation in the rare gases," J. Opt. Soc. Am. B **4**, 595 (1987).

[33] M. Ferray, A. L'Huillier, X. F. Li, L. A. Lompre, G. Mainfray, and C. Manus, "Multiple-harmonic conversion of 1064 nm radiation in rare gases," J. Phys. B At. Mol. Opt. Phys. **21**, L31–L35 (1988).

[34] J. L. Krause, K. J. Schafer, and K. C. Kulander, "High-order harmonic generation from atoms and ions in the high intensity regime," Phys. Rev. Lett. **68**, 3535–3538 (1992).

[35] A. L'Huillier and P. Balcou, "High-order harmonic generation in rare gases with a 1-ps 1053-nm laser," Phys. Rev. Lett. **70**, 774–777 (1993).

[36] P. B. Corkum, "Plasma perspective on strong field multiphoton ionization," Phys. Rev. Lett. **71**, 1994–1997 (1993).

[37] A. Rundquist, C. G. Durfee, Z. Chang, C. Herne, S. Backus, M. M. Murnane, and H. C. Kapteyn, "Phase-Matched Generation of Coherent Soft X-rays," Science **280**, 1412–1415 (1998).

[38] T. Popmintchev, M.-C. Chen, D. Popmintchev, P. Arpin, S. Brown, S. Ališauskas, G. Andriukaitis, T. Balčiunas, O. D. Mücke, A. Pugzlys, A. Baltuška, B. Shim, S. E. Schrauth, A. Gaeta, C. Hernández-García, L. Plaja, A. Becker, A. Jaron-Becker, M. M. Murnane, and H. C. Kapteyn, "Bright Coherent Ultrahigh Harmonics in the keV X-ray Regime from Mid-Infrared Femtosecond Lasers," Science **336**, 1287–1291 (2012).

[39] B. Henke, E. Gullikson, and J. Davis, "X-Ray Interactions: Photoabsorption, Scattering, Transmission, and Reflection at E = 50-30,000 eV, Z = 1-92," At. Data Nucl. Data Tables **54**, 181–342 (1993).

[40] D. Thompson, Albert C. Vaughan, *X-ray Data Booklet* (Lawrence Berkeley National Laboratory, University of California, 2009).

[41] D. Attwood, "Wave Propagation and Refractive Index at EUV and Soft X-ray Wavelengths," in *Soft X-Rays Extrem. Ultrav. Radiat.* (Cambridge University Press, 1999) pp. 55–97.

[42] D. Attwood, "Multilayer Interference Coatings," in *Soft X-Rays Extrem. Ultrav. Radiat.* (Cambridge University Press, 1999) pp. 98–122.

[43] E. J. Takahashi, H. Hasegawa, Y. Nabekawa, and K. Midorikawa, "High-throughput, high-damage-threshold broadband beam splitter for high-order harmonics in the extreme-ultraviolet region," Opt. Lett. **29**, 507 (2004).

[44] M. Puppin, Y. Deng, C. W. Nicholson, J. Feldl, N. B. M. Schröter, H. Vita, P. S. Kirchmann, C. Monney, L. Rettig, M. Wolf, and R. Ernstorfer, "Time- and angle-resolved photoemission spectroscopy of solids in the extreme ultraviolet at 500 kHz repetition rate," Rev. Sci. Instrum. **90**, 023104 (2019).

[45] O. Pronin, V. Pervak, E. Fill, J. Rauschenberger, F. Krausz, and A. Apolonski, "Ultrabroadband efficient intracavity XUV output coupler," Opt. Express **19**, 10232 (2011).

[46] K. Yao, F. Willems, C. von Korff Schmising, C. Strüber, P. Hessing, B. Pfau, D. Schick, D. Engel, K. Gerlinger, M. Schneider, and S. Eisebitt, "A table-top setup for ultrafast helicity-dependent and element-specific absorption spectroscopy and scattering in the extreme ultraviolet spectral range," Rev. Sci. Instrum. **91**, 093001 (2020).

[47] M. Keunecke, C. Möller, D. Schmitt, H. Nolte, G. S. M. Jansen, M. Reutzel, M. Gutberlet, G. Halasi, D. Steil, S. Steil, and S. Mathias, "Time-resolved momentum microscopy with a 1 MHz high-harmonic extreme ultraviolet beamline," Rev. Sci. Instrum. **91**, 063905 (2020).

[48] F. R. Powell, "Thin film filter performance for extreme ultraviolet and x-ray applications," Opt. Eng. **29**, 614 (1990).

[49] M. Morita, T. Ohmi, E. Hasegawa, M. Kawakami, and M. Ohwada, "Growth of native oxide on a silicon surface," J. Appl. Phys. **68**, 1272–1281 (1990).

[50] D. L. Windt, "IMD—Software for modeling the optical properties of multilayer films," Comput. Phys. **12**, 360 (1998).

[51] J. Rebellato, S. de Rossi, X. Zhang, F. Auchère, E. Meltchakov, F. Delmotte, and R. Soufli, "Analyses of tabulated optical constants for thin films in the EUV range and application to solar physics multilayer coatings," in *Adv. Opt. Thin Film. VI*, edited by M. Lequime, H. A. Macleod, and D. Ristau (SPIE, 2018) p. 64.

[52] E. Palik, ed., *Handbook of Optical Constants of Solids Vol. 1* (Academic Press, 1985).

[53] E. Palik, ed., *Handbook of Optical Constants of Solids Vol. 2* (Academic Press, 1991).

[54] M. Pascolini, S. Bonora, A. Giglia, N. Mahne, S. Nannarone, and L. Poletto, "Gratings in a conical diffraction mounting for an extreme-ultraviolet time-delay-compensated monochromator," Appl. Opt. **45**, 3253 (2006).

[55] C. Tarrio, R. F. Berg, T. B. Lucatorto, F. G. Eparvier, A. R. Jones, B. Templeman, D. L. Woodraska, and M. Dominique, "Evidence Against Carbonization of the Thin-Film Filters of the Extreme Ultraviolet Variability Experiment Onboard the Solar Dynamics Observatory," Sol. Phys. **296**, 55 (2021).

[56] M. R. Howells, "Mirrors for Synchrotron-Radiation Beamlines," in *New Dir. Res. with Third-Generation Soft X-Ray Synchrotron Radiat. Sources* (Springer Netherlands, Dordrecht, 1994) pp. 359–385.

[57] F. Frassetto, A. Trabattoni, S. Anumula, G. Sansone, F. Calegari, M. Nisoli, and L. Poletto, "High-throughput beamline for attosecond pulses based on toroidal mirrors with microfocusing capabilities," Rev. Sci. Instrum. **85**, 103115 (2014).

[58] K. Klementiev and R. Chernikov, "Powerful scriptable ray tracing package xrt," in *Adv. Comput. Methods X-Ray Opt. III*, edited by M. Sanchez del Rio and O. Chubar (SPIE, 2014) p. 92090A.

[59] C. Valentin, D. Douillet, S. Kazamias, T. Lefrou, G. Grillon, F. Augé, G. Mullot, P. Balcou, P. Mercère, and P. Zeitoun, "Imaging and quality assessment of high-harmonic focal spots," Opt. Lett. **28**, 1049 (2003).

[60] L. Le Déroff, P. Salières, and B. Carré, "Beam-quality measurement of a focused high-order harmonic beam," Opt. Lett. **23**, 1544 (1998).

[61] H. Motoyama, A. Iwasaki, Y. Takei, T. Kume, S. Egawa, T. Sato, K. Yamanouchi, and H. Mimura, "Broadband nano-focusing of high-order harmonics in soft X-ray region with ellipsoidal mirror," Appl. Phys. Lett. **114**, 241102 (2019).

[62] A. Korobenko, S. Rashid, C. Heide, A. Y. Naumov, D. A. Reis, P. Berini, P. B. Corkum, and G. Vampa, "In-Situ Nanoscale Focusing of Extreme Ultraviolet Solid-State High Harmonics," Phys. Rev. X **12**, 041036 (2022).

[63] W. C. Walker, N. Wainfan, and G. L. Weissler, "Photoelectric Yields in the Vacuum Ultraviolet," J. Appl. Phys. **26**, 1366–1371 (1955).

[64] A. J. Blodgett and W. E. Spicer, "Experimental Determination of the Density of States in Nickel," Phys. Rev. **146**, 390–402 (1966).

[65] I. Kuznetsov, J. Filevich, F. Dong, M. Woolston, W. Chao, E. H. Anderson, E. R. Bernstein, D. C. Crick, J. J. Rocca, and C. S. Menoni, "Three-dimensional nanoscale molecular imaging by extreme ultraviolet laser ablation mass spectrometry," Nat. Commun. **6**, 6944 (2015).

[66] R. G. Wilson, "Vacuum Thermionic Work Functions of Polycrystalline Be, Ti, Cr, Fe, Ni, Cu, Pt, and Type 304 Stainless Steel," J. Appl. Phys. **37**, 2261–2267 (1966).

[67] A. J. Blodgett and W. E. Spicer, "Experimental Determination of the Optical Density of States in Iron," Phys. Rev. **158**, 514–523 (1967).

[68] J. Ladislas Wiza, "Microchannel plate detectors," Nucl. Instruments Methods **162**, 587–601 (1979).

[69] T. J. Prosa and E. Oltman, "Study of LEAP 5000 Deadtime and Precision via Silicon Pre-Sharpened-Microtip™ Standard Specimens," Microsc. Microanal. **28**, 1019–1037 (2022).

[70] P. Dumas, S. Duguay, J. Borrel, F. Hilario, and D. Blavette, "Atom probe tomography quantification of carbon in silicon," Ultramicroscopy **220**, 113153 (2021).

[71] F. Meisenkothen, T. F. Kelly, E. Oltman, J. H. Bunton, L. Renaud, and D. J. Larson, "Using Mass Resolving Power as a Performance Metric in the Atom Probe," Microsc. Microanal. **22**, 680–681 (2016).

[72] L. Miaja-Avila, B. W. Caplins, A. N. Chiaramonti, P. T. Blanchard, M. D. Brubaker, A. V. Davydov, D. R. Diercks, B. P. Gorman, A. Rishinaramangalam, D. F. Feezell, K. A. Bertness, and N. A. Sanford, "Extreme Ultraviolet Radiation Pulsed Atom Probe Tomography of III-Nitride Semiconductor Materials," J. Phys. Chem. C **125**, 2626–2635 (2021).

[73] Q. Zhang, B. Klein, N. A. Sanford, and A. N. Chiaramonti, "Comparative Apex Electrostatics of Atom Probe Tomography Specimens," J. Electron. Mater. **50**, 3022–3029 (2021).

[74] D. R. Diercks, B. P. Gorman, R. Kirchhofer, N. Sanford, K. Bertness, and M. Brubaker, "Atom probe tomography evaporation behavior of C-axis GaN nanowires: Crystallographic, stoichiometric, and detection efficiency aspects," J. Appl. Phys. **114**, 184903 (2013).

[75] L. Mancini, N. Amirifar, D. Shinde, I. Blum, M. Gilbert, A. Vella, F. Vurpillot, W. Lefebvre, R. Lardé, E. Talbot, P. Pareige, X. Portier, A. Ziani, C. Davesnne, C. Durand, J. Eymery, R. Butté, J.-F. Carlin, N. Grandjean, and L. Rigutti, "Composition of Wide Bandgap Semiconductor Materials and Nanostructures Measured by Atom Probe Tomography and Its Dependence on the Surface Electric Field," J. Phys. Chem. C **118**, 24136–24151 (2014).

[76] R. J. H. Morris, R. Cuduvally, D. Melkonyan, C. Fleischmann, M. Zhao, L. Arnoldi, P. van der Heide, and W. Vandervorst, "Toward accurate composition analysis of GaN and AlGaN using atom probe tomography," J. Vac. Sci. Technol. B, Nanotechnol. Microelectron. Mater. Process. Meas. Phenom. **36**, 03F130 (2018).

[77] E. D. Russo, I. Blum, J. Houard, M. Gilbert, G. Da Costa, D. Blavette, and L. Rigutti, "Compositional accuracy of atom probe tomography measurements in GaN: Impact of experimental parameters and multiple evaporation events," Ultramicroscopy **187**, 126–134 (2018).

[78] L. Rigutti, B. Bonef, J. Speck, F. Tang, and R. Oliver, "Atom probe tomography of nitride semiconductors," Scr. Mater. **148**, 75–81 (2018).

[79] R. J. Morris, R. Cuduvally, D. Melkonyan, M. Zhao, P. van der Heide, and W. Vandervorst, "Atom probe of GaN/AlGaN heterostructures: The role of electric field, sample crystallography and laser excitation on quantification," Ultramicroscopy **206**, 112813 (2019).

[80] D. Larson, R. Alvis, D. Lawrence, T. Prosa, R. Ulfig, D. Reinhard, P. Clifton, S. Gerstl, J. Bunton, D. Lenz, T. Kelly, and K. Stiller, "Analysis of Bulk Dielectrics with Atom Probe Tomography," Microsc. Microanal. **14**, 1254–1255 (2008).